Beyond the effective length: how to analyze magnetic interference patterns of thin-film planar Josephson junctions with finite lateral dimensions

Fermin, R.; Wit, B. de; Aarts, J.

Note: To cite this publication please use the final published version (if applicable).

Beyond the effective length: How to analyze magnetic interference patterns of thin-film planar Josephson junctions with finite lateral dimensions

R. Fermin ●, B. de Wit, and J. Aarts

Huygens-Kamerlingh Onnes Laboratory, Leiden University, P.O. Box 9504, 2300 RA Leiden, The Netherlands

The magnetic-field-dependent critical current $I_c(B)$ of a Josephson junction is determined by the screening currents in its electrodes. In macroscopic junctions, a local vector potential drives the currents; however, in thin-film planar junctions, with electrodes of finite size and various shapes, they are governed by nonlocal electrodynamics. This complicates the extraction of parameters such as the geometry of the effective junction area, the effective junction length, and the critical current density distribution from the $I_c(B)$ interference patterns. Here, we provide a method to tackle this problem by simulating the phase differences that drive the shielding currents and use those to find $I_c(B)$. To this end, we extend the technique proposed by Clem [Phys. Rev. B **81**, 144515 (2010)] to find $I_c(B)$ for Josephson junctions separating a superconducting strip of length L and width W with rectangular, ellipsoid, and rhomboid geometries. We find the periodicity of the interference pattern (ΔB) to have geometry-independent limits for $L \gg W$ and $L \ll W$. By fabricating elliptically shaped superconductor–normal-metal–superconductor junctions with various aspect ratios, we experimentally verify the L/W dependence of ΔB. Finally, we incorporate these results to correctly extract the distribution of critical currents in the junction by the Fourier analysis of $I_c(B)$, which makes these results essential for the correct analysis of topological channels in thin-film planar Josephson junctions.

I. INTRODUCTION

Planar Josephson junctions are ubiquitous in modern solid-state physics research, with examples ranging from topological junctions [1–3], high-critical-temperature (grain boundary) junctions [4,5], gated junctions that control supercurrent flow [6,7], graphene-based junctions [8,9], magnetic field sensors [10–12], and junctions with a ferromagnetic weak link [13–15]. A major tool in analyzing these junctions experimentally is the magnetic interference pattern observed in the critical current [$I_c(B)$], the shape and periodicity of which can reveal, using the Fourier transform, information about the underlying distribution of critical current in the weak link [16]. Often this Fourier analysis is carried out in terms of an effective junction length, given, for macroscopic junctions, by $2\lambda + d$, where λ is the London penetration depth and d is the thickness of the weak link. This effective length originates from the Meissner effect. However, when the junction is formed between two superconducting thin films, with a thickness below λ, the shielding currents running along the junction, responsible for the shape and periodicity of the magnetic interference of the critical current $I_c(B)$, are no longer determined by the Meissner effect in its macroscopic form (i.e., by the local vector potential). Rather, they are determined by nonlocal electrodynamic effects [17–20].

In numerous theoretical and experimental studies, it was found that in thin-film planar junctions, $I_c(B)$ becomes completely independent of λ and is solely determined by the geometry of the sample [20–24]. Moreover, Clem provided a method to calculate $I_c(B)$ for planar junctions that are also restricted in their lateral size (i.e., a Josephson junction separating a rectangular superconducting strip of width W and length L in two halves) [23]. As experimental studies often deal with finite-size geometries, his theory is highly topical at the moment.

This paper bridges the gap between predicting the $I_c(B)$ of thin-film planar junctions featuring finite lateral geometry and the correct analysis of the experimental interference patterns used to extract the current density distribution. First we review the technique proposed by Clem and extend on his work by covering two more geometries: the ellipse and the rhomboid. We calculate $I_c(B)$ for these geometries, extract the periodicity of the interference pattern (ΔB) for different ratios of L/W, and find ΔB to have two geometry-independent limits for $L \gg W$ and $L \ll W$. By fabricating elliptically shaped superconductor–normal-metal–superconductor (S-N-S) junctions with different ratios L/W, we experimentally verify the geometry dependence of ΔB. Finally, we adapt the well-known Fourier relation between $I_c(B)$ and the critical current density distribution for use on laterally finite thin-film planar junctions. We find that altering the Fourier transform is crucial for predicting the location of possible current channels in thin-film planar junctions.
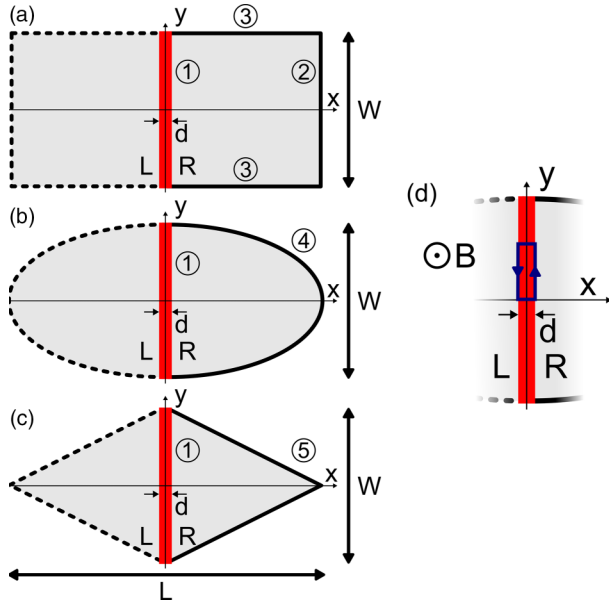
FIG. 1. Schematics of the three geometries used for calculating $I_c(B)$, being (a) the rectangle, (b) the ellipse, and (c) the rhombus. The schematics resemble superconducting thin films of width W and length L, which are separated by a normal-metal junction of width d (colored red). The numbers indicate different sections of the right electrode edge. The boundary conditions of the calculations for these are summarized in Table I. In (d) we show a zoom of the junction area under the magnetic induction $\boldsymbol{B} = B\hat{z}$. The dark blue path is used as loop integral to determine $I_c(B)$. L and R stand for left and right electrode respectively.

II. REVIEW OF THE CLEM MODEL

We consider a normal-metal Josephson junction (dimensions W_{JJ} and d) that divides a symmetric superconducting thin film, having dimensions L and W, into two halves. Figure 1 shows a schematic of three such films, having different geometries. The junction, colored red in Fig. 1, runs along the y direction from $-W/2$ to $W/2$ (i.e., $W_{JJ} = W$). Since we examine the thin-film limit, the screening current density is assumed to be uniform along the thickness of the film, which effectively reduces the problem to a two-dimensional (2D) one. We specifically consider the junction to be in the short-junction limit, as the model by Clem treats an infinitesimally thin insulating tunnel junction. Furthermore, it is assumed that the electrode dimensions are smaller than the Pearl length, given by

$$\Lambda = \frac{2\lambda^2}{t_{\text{film}}}, \tag{1}$$

where t_{film} is the thickness of the superconducting films. This implies that the self-fields originating from the screening currents are far smaller than the applied external field. Additionally, we assume that the junction is in the narrow limit, meaning that the junction is less wide than the Josephson penetration length, which for planar junctions in the thin-film limit is the given by [20,21,23]

$$l = \frac{\Phi_0 t_{\text{junc}} W}{4\pi \mu_0 \lambda^2 I_c(0)}. \tag{2}$$

Here, t_{junc} is the thickness of the junction (not necessarily equal to the thickness of the film), $I_c(0)$ is its critical current at zero magnetic field, μ_0 is the vacuum permeability, and Φ_0 is the magnetic flux quantum.

In order to calculate $I_c(B)$, we assume a sinusoidal current-phase relation $J_x = J_c \sin\varphi(y)$, where $\varphi(y)$ is the gauge-invariant phase difference over the junction, which depends on the location along the junction. It can be evaluated within the framework of Ginzburg-Landau theory by considering the second Ginzburg-Landau equation, which is given as

$$\boldsymbol{J} = -\frac{\Phi_0}{2\pi\mu_0\lambda^2}\left(\frac{2\pi}{\Phi_0}\boldsymbol{A} + \boldsymbol{\nabla}\gamma\right) = \frac{\Phi_0}{2\pi\mu_0\lambda^2}\theta. \tag{3}$$

Here, A is the vector potential corresponding to the applied magnetic field ($\boldsymbol{B} = \boldsymbol{\nabla} \times \boldsymbol{A}$), and γ is the gauge-covariant phase of the wave function describing the superconducting order parameter (given by $\Psi = \Psi_0 e^{i\gamma}$ [25]). Finally, θ is the gauge-invariant phase gradient (required by the fact that J is a gauge-invariant property). $\varphi(y)$ is then given by integrating θ across the junction:

$$\varphi(y) = \gamma\left(-\frac{d}{2}, y\right) - \gamma\left(\frac{d}{2}, y\right) - \frac{2\pi}{\Phi_0}\int_{-d/2}^{d/2} A_x(x, y)\, dx. \tag{4}$$

In Fig. 1(d), we sketch a zoom of a junction, where we specify an integration contour under a magnetic induction of $\boldsymbol{B} = B\hat{z}$. By integrating $\boldsymbol{\nabla}\gamma$ along this contour and realizing that $\int_C \boldsymbol{\nabla}\gamma\, d\boldsymbol{l} = 2\pi n$, where n is an integer and $\sin(\varphi + 2\pi n) = \sin(\varphi)$, we find

$$\varphi(y) = \varphi(0) + \frac{2\pi}{\Phi_0}\left[ydB + 2\mu_0\lambda^2\int_0^y J_y\left(\frac{d}{2}, y'\right)dy'\right]. \tag{5}$$

Here, we have used the Stokes theorem to evaluate the flux entering the contour and used the fact that the electrodes are mirror symmetric [$J_y(\frac{d}{2}, y) = -J_y(-\frac{d}{2}, y)$]. For macroscopic junctions, $J_{y,R}(\frac{d}{2}, y') = \frac{B\mu_0}{\lambda_L}$ resulting from the the Meissner effect, leading to $\varphi(y) = \varphi(0) + \frac{2\pi(2\lambda+d)B}{\Phi_0}y$, where we recognize the effective junction length. Since the junctions considered here are in the thin-film limit, we take a different approach in evaluating $J_y(\frac{d}{2}, y')$. First note that the super-current is conserved and therefore $\boldsymbol{\nabla} \cdot \boldsymbol{J} = 0$. By choosing the convenient gauge $\boldsymbol{A} = -yB\hat{x}$, we find $\boldsymbol{\nabla} \times \boldsymbol{A} = B\hat{z}$ and $\boldsymbol{\nabla} \cdot \boldsymbol{A} = 0$. Therefore the divergence of the second Ginzburg-Landau equation [Eq. (3)] reduces to

$$\nabla^2\gamma = 0. \tag{6}$$

Therefore we mapped the second Ginzburg-Landau equation onto the Laplace equation. With sufficient boundary conditions, it can be solved for a unique solution, which allows us to calculate $J_y(\frac{d}{2}, y)$. The boundary conditions arise from the prerequisite that no supercurrent can exit the sample at its outer boundaries. Furthermore, we assume a weak Josephson coupling, meaning that the shielding currents in the electrodes are far larger than the Josephson currents between the electrodes, which we approximate as $J_x(\frac{d}{2}, y) = 0$. Therefore we can write

$$\boldsymbol{J} \cdot \hat{\boldsymbol{n}}_R = 0, \tag{7}$$

where $\hat{n}_R$ is the unit vector, normal to the outer edges of the right electrode. Combined with the second Ginzburg-Landau equation, this leads to a set of Neumann boundary conditions:

$$(\nabla \gamma) \cdot \hat{n}_R = -\frac{2\pi}{\Phi_0} A \cdot \hat{n}_R, \qquad (8)$$

which is sufficient to solve for $\gamma(x, y)$. Next, Eq. (5) allows us to find the gauge-invariant phase difference over the junction $\varphi(y)$. Note that we have conveniently chosen $A_y = 0$. We then find

$$2\mu_0 \lambda^2 \int_0^y J_y\left(\frac{d}{2}, y'\right) dy' = 2\gamma\left(\frac{d}{2}, y\right). \qquad (9)$$

Therefore $\varphi(y)$ is given by the simple expression

$$\varphi(y) = \varphi(0) + \frac{2\pi d B}{\Phi_0} y + 2\gamma\left(\frac{d}{2}, y\right). \qquad (10)$$

Next, the current across the junction is given by $\int J \, dS$, yielding

$$I(B) = \int_{-W/2}^{W/2} t_{\text{junc}} J_c \sin\left[\varphi(0) + \frac{2\pi d B}{\Phi_0} y + 2\gamma\left(\frac{d}{2}, y\right)\right] dy. \qquad (11)$$

We assume that the critical current density at zero field is distributed uniformly over the junction, yielding $J_c = \frac{I_c(0)}{t_{\text{junc}} W}$. Also, note that $\varphi(0)$ is independent of y and therefore is merely a phase factor. The critical current is reached if we current-bias the junction by setting $\varphi(0) = \pi/2$, from which follows

$$\frac{I_c(B)}{I_c(0)} = \frac{1}{W} \left| \int_{-W/2}^{W/2} \cos\left[\frac{2\pi d B}{\Phi_0} y + 2\gamma\left(\frac{d}{2}, y\right)\right] dy \right|. \qquad (12)$$

We see that finding $I_c(B)$ becomes equal to a boundary condition problem of solving the Laplace equation in the geometry of the electrodes. Indeed, the solution is completely determined by the geometry of the sample and is independent of λ.

III. COMPARING DIFFERENT GEOMETRIES

As it is not trivial to find a general analytical solution to the boundary problem of Eq. (6) for the ellipsoid and rhomboid geometries, we solve the Laplace equation numerically using COMSOL MULTIPHYSICS version 5.4. We define the right-electrode geometry in 2D, divided into a triangular grid. Crucial for correctly solving Eq. (6) is a grid size that is small enough to capture small changes in γ and, on the edges, $\hat{n}_R$. We found a maximum element size (i.e., the grid edge size) of $0.01 \ln(1 + L/W)$ nm to be a good compromise between computation time and precision. Using trigonometry, we evaluate $A \cdot \hat{n}_R$ for each geometry and list the corresponding boundary conditions in Table I (the numbering in Table I corresponds to the numbers in Fig. 1). In the Appendix, we provide a full derivation of each of the boundary conditions, while the Supplemental Material contains the COMSOL application file [26].

TABLE I. The Neumann boundary conditions for each electrode boundary, listed by the numbering used in Fig. 1.

Boundary	$(\nabla \gamma) \cdot \hat{n}_\Omega$
1	$\frac{2\pi B}{\Phi_0} y$
2	$-\frac{2\pi B}{\Phi_0} y$
3	0
4	$\frac{2\pi B}{\Phi_0} \frac{Wxy}{L\sqrt{(\frac{Wx}{L})^2 + (\frac{Ly}{W})^2}}$
5	$-\frac{2\pi B}{\Phi_0} \frac{Wy}{\sqrt{W^2 + L^2}}$

A. Simulation results

Clem showed that the analytical solution for the rectangular geometry is an infinite series of sines and hyperbolic tangents [23]. For the rectangle, this leads to the maximum in $\gamma(\frac{d}{2}, y)$ occurring at $W/2$, which can be approximated as

$$\gamma\left(\frac{d}{2}, \frac{W}{2}\right) = \frac{7\zeta(3)}{\pi^2} \frac{BW^2}{\Phi_0} \tanh\left(\frac{\pi^3}{28\zeta(3)} \frac{L}{W}\right). \qquad (13)$$

Here, ζ is the Riemann zeta function. Now we generalize this approximation to include the other geometries. We find that the simulated $\gamma(\frac{d}{2}, y)$ universally follows

$$\gamma\left(\frac{d}{2}, y\right) = \frac{7\zeta(3)}{\pi^2} \frac{BW^2}{\Phi_0} \tanh\left(\frac{\pi^3}{28\zeta(3)} \frac{A}{W^2}\right) f\left(\frac{y}{W}\right), \qquad (14)$$

where $f(\frac{y}{W})$ is a dimensionless function defined by the specific geometry and A is the total surface area of the electrodes (i.e., the combined area of the left and right electrodes). Note that we have substituted $\frac{L}{W}$ in the argument of the hyperbolic tangent for $\frac{A}{W^2}$; the reason for this choice will become apparent below when discussing the period of the $I_c(B)$ pattern. Figure 2(a) shows the calculated $\gamma(x, y)$ for a disk geometry, normalized to the applied magnetic field and width of the electrodes $\gamma \Phi_0 / BW^2$. We plot $f(\frac{y}{W})$ for this disk in Fig. 2(b). By evaluating the integral of Eq. (12) numerically for different values of B, we calculate the interference pattern of a disk-shaped junction [Fig. 2(c)]. The pattern resembles a Fraunhofer pattern at first sight. However, the peak height decreases less strongly than $1/B$, and the width of the middle lobe is not twice the width of the sidelobes. In the inset of Fig. 2(c), we plot the width of the nth sidelobe (ΔB_n); the width increases and reaches an asymptotic value for large n.

In order to compare the interference patterns of junctions of different geometry, we define the period of the oscillations to be the width of the fifth sidelobe ($\Delta B = \Delta B_5$). In the inset of Fig. 2(c), this is shown by the vertical reference line. The width of the fifth sidelobe is not only sufficiently close to the asymptotic value but also experimentally accessible without the need for large magnetic fields. We now compare the periodicity of the interference patterns for different geometries by plotting the dimensionless value $\Delta BW^2/\Phi_0$ as a function of the aspect ratio L/W in Fig. 3(a) on a log-log scale. First, we find the results obtained on the rectangular junction to match the analytical results obtained by Clem [23]. Furthermore, the periodicity of the pattern increases as the sample dimensions are diminished. Finally, we evaluate the width of the junction
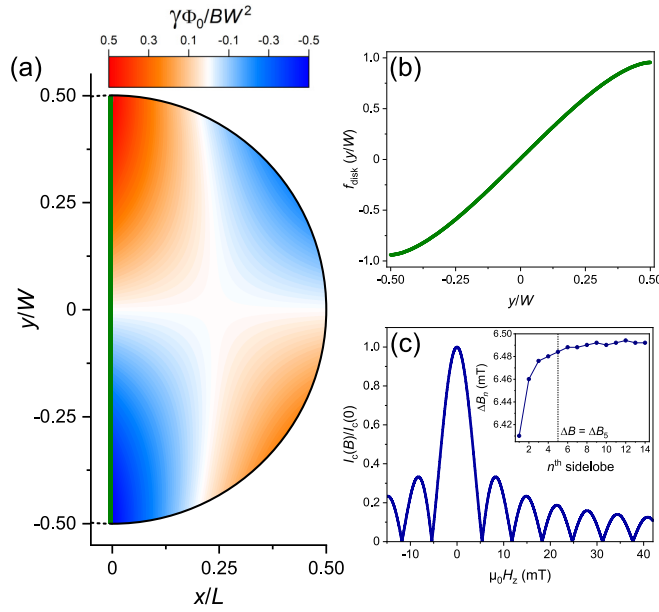
FIG. 2. (a) Gauge-covariant phase simulated in the right electrode for a disk-shaped planar Josephson junction, normalized to the applied magnetic field and width of the junction $\gamma \Phi_0 / BW^2$. The junction is shown as a green line. This result allows for extracting the gauge-covariant phase along the junction. It follows the scaling of Eq. (14), and it is determined by a dimensionless function, which is plotted in (b). (c) Interference pattern calculated using the result in (a) by numerically evaluating Eq. (12) for different values of B. The typical interference pattern looks like a Fraunhofer pattern at first sight. However, the peak height decreases less strongly than $1/B$, and the width of the sidelobes is larger than half of the middle lobe, which is 10.76 mT wide. Furthermore, the width of the nth sidelobe increases and reaches an asymptotic value for large values of n, which is evident from the inset of (c), where we plot the width of the nth sidelobe. The width of the fifth sidelobe is used for comparisons between simulations and experiments.

(d) to be irrelevant in determining ΔB. Specifically, its contribution to the period is in the µT range for realistic sizes of d. The consequence is that ΔB is determined by the maximum of γ, i.e., $\gamma(\frac{d}{2}, \frac{W}{2})$.

ΔB reaches asymptotic values for the limits $L \gg W$ and $L \ll W$ for all three geometries. The value of ΔB becomes geometry independent in these limits, as revealed by rescaling the results from Fig. 3(a) to an $\frac{A}{W^2}$ dependence, displayed in Fig. 3(b). In the first limit, $L \gg W$, all three geometries become an infinite superconducting strip. Here, we retrieve $\Delta B = 1.842 \Phi_0 / W^2$, which matches the literature [22,23]. In this limit, we find $\gamma(\frac{d}{2}, y)$ to follow

$$\gamma\left(\frac{d}{2}, y\right) = \frac{7\,\zeta(3)}{\pi^2} \frac{BW^2}{\Phi_0} f_{\text{strip}}\left(\frac{y}{W}\right) \qquad (15)$$

$$= \frac{\pi}{2} \frac{1}{1.842} \frac{BW^2}{\Phi_0} f_{\text{strip}}\left(\frac{y}{W}\right), \qquad (16)$$

where $f_{\text{strip}}(\frac{y}{W})$ is a dimensionless function running from -1 to 1, plotted in Fig. 4(a). In the other limit, $L \ll W$, Eq. (14)
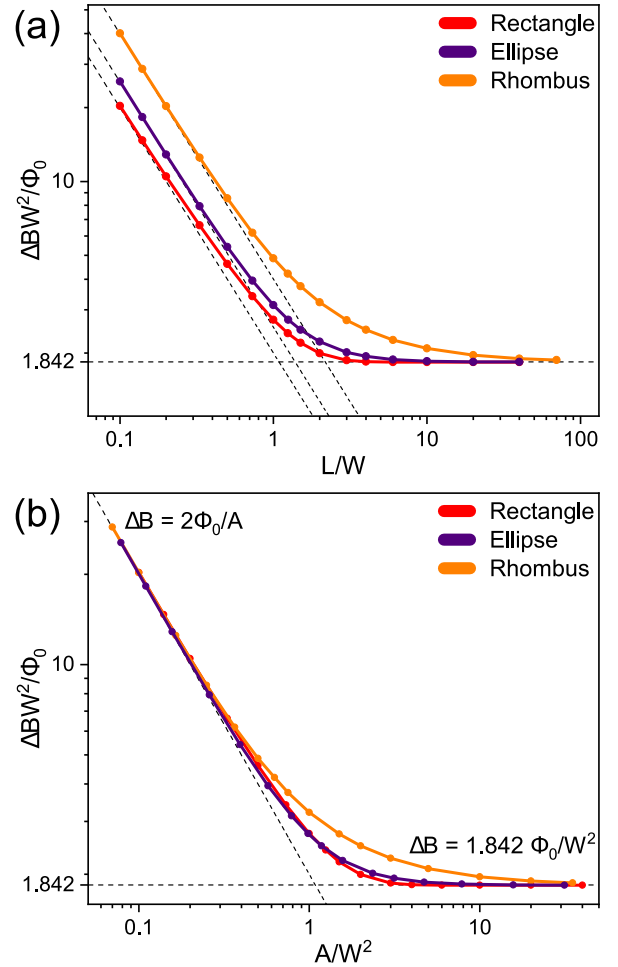

FIG. 3. Dimensionless measure of the period ΔB (the width of the fifth sidelobe) of the calculated interference pattern $I_c(B)$ for the three geometries. In (a) we plot this value on a log-log scale vs the aspect ratio L/W, and in (b) it is plotted vs the total electrode area A (i.e., the combined area of the left and right electrodes), scaled by W^2. (b) reveals two limits for ΔB for $L \gg W$ and $L \ll W$. The first corresponds to the limit of an infinite superconducting strip $\Delta B = 1.842\Phi_0 / W^2$, whereas in the latter we find $\Delta B = 2\Phi_0 / A$. In contrast to ΔB, $I_c(B)$ itself is not geometry independent in this limit.

reduces to

$$\gamma\left(\frac{d}{2}, y\right) = \frac{\pi A B}{4 \Phi_0} f\left(\frac{y}{W}\right) = \frac{\pi}{2} \frac{AB}{2\Phi_0} f\left(\frac{y}{W}\right). \qquad (17)$$

Figure 4(b) shows $f(\frac{y}{W})$ in the limit $L \ll W$, for all three geometries. Since the maximum of $f(\frac{y}{W})$ becomes independent of the underlying geometry and equal to unity, we find a geometry-independent period, where $\Delta B = 2\Phi_0 / A$. We can generalize this concept to find a general expression for ΔB:

$$\Delta B = \frac{\pi}{2} \frac{1}{\max(\gamma/B)} = \frac{\pi}{2} \frac{B}{\gamma\left(\frac{d}{2}, \frac{W}{2}\right)}. \qquad (18)$$

Note that $\max[f(\frac{y}{W})] \approx 1$ for all ratios L/W, and thus Eq. (18) can serve as a good approximation for ΔB. Therefore we justify the relation of Eq. (14) as it demonstrates the emerging universal limits where $\Delta B = 2\Phi_0 / A$ and $\Delta B = 1.842\Phi_0 / W^2$,
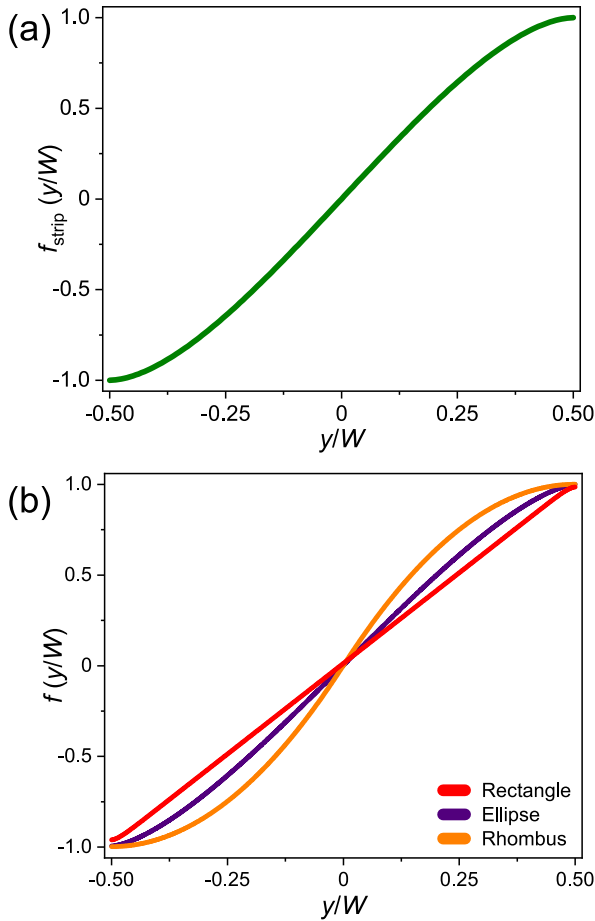
FIG. 4. Dimensionless scaling functions $f(\frac{y}{W})$ from Eq. (14), for the limit $L \gg W$ in (a) and $L \ll W$ in (b). The maximum of these functions is located at $y = |W/2|$ and equals unity. Therefore ΔB [large-n limit of the nth sidelobe of $I_c(B)$] is universal for these limits. However, for the limit $L \ll W$, $f(\frac{y}{W})$ is not geometry independent, which entails that $I_c(B)$ is not geometry independent either, in this limit.

as well as providing a good approximation of ΔB between the limiting cases.

Although ΔB is geometry independent in the limit $L \ll W$, $I_c(B)$ itself is not universal in this limit. This is caused by the fact that $f(\frac{y}{W})$ differs between geometries for $y \neq |W/2|$ [see Fig. 4(b)]. For the rectangular geometry, for example, this function is linear in y: $f(\frac{y}{W}) = \frac{2y}{W}$. Therefore we retrieve the Fraunhofer pattern, where $L_{\text{eff}} = L/2 + d$. The effective length equals the length of a single superconducting electrode plus the junction length. This can be understood by considering that the screening currents trace loops in the electrodes, that reduce to two parallel and opposite current tracks, when $L \ll W$. $\gamma(\frac{d}{2}, y)$ in the rhomboid geometry is radically different; it is well approximated by a sine function: $f(\frac{y}{W}) = \sin(\frac{\pi y}{W})$. This leads to an interference pattern that is far closer to the pattern shown in Fig. 2(c), and not a Fraunhofer pattern. In conclusion, the shape and periodicity of the $I_c(B)$ pattern for low magnetic fields is independent of ΔB, which is universal for $L \ll W$.

B. Comparison with experiments

In order to verify the dependence on the geometry, we fabricate five ellipse-shaped planar S-N-S junctions for different ratios of L/W. Besides, we make a rectangular-shaped junction with dimensions well within the $L \gg W$ limit.

First, a four-probe contact geometry is patterned on Si substrates using electron-beam lithography. Next, a bilayer of Ag (20 nm) and MoGe (55 nm) is deposited by sputter deposition. Subsequently, we use focused ion beam (FIB) milling to structure elliptical devices in the bilayer. By applying an ultralow beam current of 1.5 pA, the weak link is formed by a line cut in the MoGe layer at the center of the device. This completely removes the superconductor on top, but leaves a normal-metal connection. The resulting trench separates the MoGe electrodes by a roughly 20-nm weak link, allowing Josephson coupling in this S-N-S system. Similar junctions, featuring a ferromagnetic layer, were fabricated in this manner, to study the interplay between supercurrents and ferromagnetic spin textures [13,14,27]. Figures 5(a) and 5(c) show false-color electron micrographs of two such devices, for $L = W$ and $L = 4W$, respectively.

Two corresponding interference patterns obtained on the samples in Figs. 5(a) and 5(c) are shown in Figs. 5(b) and 5(d). Clearly, the period of the interference patterns scales with L/W. However, we find that the middle peak is twice the width of the neighboring ones and the amplitude of the sidelobes of the $I_c(B)$ pattern feature a similar width, instead of the asymptotic behavior predicted by our theory [see Fig. 2(c)]. This can be explained by considering that $l \approx 100$ nm (Eq. (2); based on $\lambda = 535$ nm [29]), which is small with respect to W. Our samples are therefore not in the narrow-junction limit and allow Josephson vortices to stabilize in the junction. The width of the middle lobe can therefore not be predicted by our theory. However, Boris *et al.* have shown that ΔB_n for large n follows the predictions of nonlocal electrodynamics [20]. Therefore we can compare the measured $\Delta B = \Delta B_5$ with our theoretical model.

To compare the period of the $I_c(B)$ pattern with our theory, we plot ΔB for all measured samples along with the calculated values in Fig. 6. With the blue star symbol, we also mark the periodicity of the Co-based superconductor-ferromagnet-superconductor (S-F-S) disk junctions discussed elsewhere [14]. Although there is a constant offset between the measured periodicity and the calculated values, the overall trend is well predicted.

This constant offset is due to a trivial side effect of the FIB structuring method: Some parts of the bilayer (i.e., the edges of the device) mill faster than the bulk of the material. Consequently, notches develop on the side of the device when fabricating the trench. These notches make the width of the weak link (W_{JJ}) shorter than the width of the electrodes (W), which can result in a constant offset between experiments and the simulations, where it is assumed that $W_{\text{JJ}} = W$. In order to show that we reach the geometry-independent limit for $L \gg W$, we have fabricated a bar-shaped sample with $L/W > 10$. In the Supplemental Material we present a scanning electron micrograph of this device accompanied by the interference pattern obtained on this sample [26]. In this limit we expect $\Delta B W_{\text{JJ}}^2 / \Phi_0 = 1.842$ [10,12]. By inspection of the
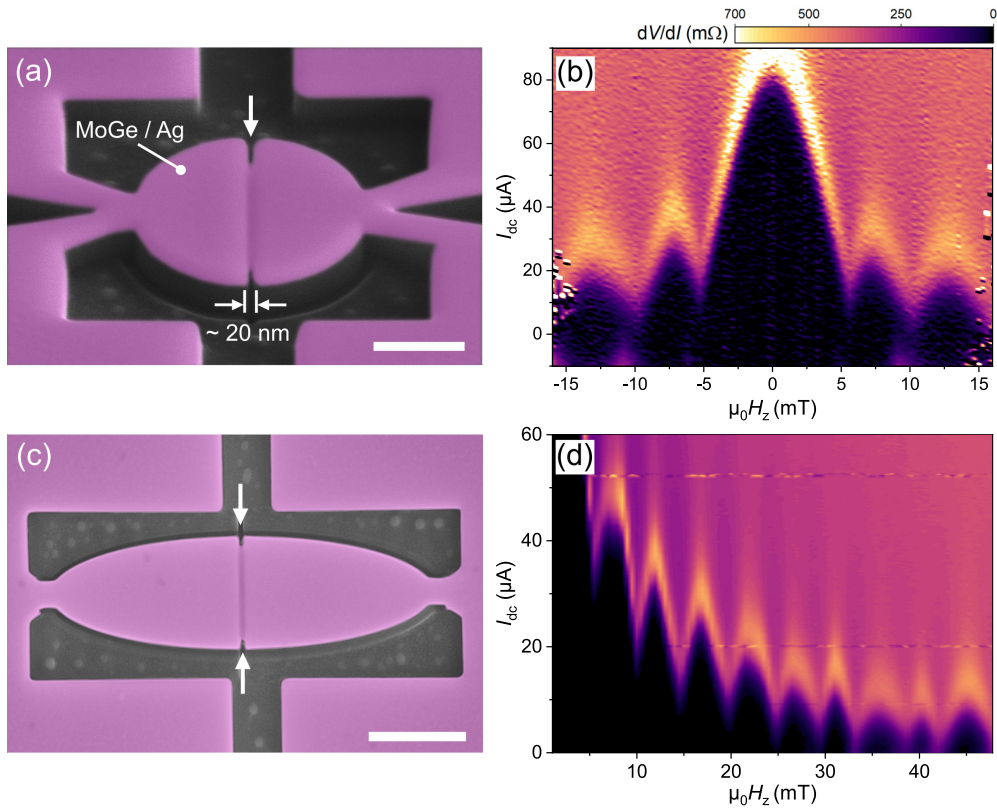
FIG. 5. Two S-N-S junction samples with a circular and ellipsoid geometry, produced from an Ag/MoGe bilayer and their corresponding $I_c(B)$ patterns, obtained at 2.5 K. (a) A false-color electron micrograph of a disk-shaped sample, viewed at an angle. The white arrows indicate the junction. Note the notches on the side of the sample due to an increased milling rate at the edges of the disk. The scale bar equals 500 nm. (b) The corresponding $I_c(B)$ displayed as a dV/dI color map. As expected, the peak height of the sidelobes is decreasing less rapidly than $1/B$. In contrast to the calculated pattern in Fig. 2(c), the middle peak is twice as wide as the neighboring ones. (c) A top-view false-color electron micrograph of an ellipse-shaped junction. Again we indicate the junction, and notches, with white arrows; the scale bar represents 1 μm. (d) The corresponding interference pattern as a dV/dI color map, which is used to extract the periodicity of the oscillations [28].

scanning electron micrograph we have extracted W_{JJ} for the bar-shaped sample, which leads to $\Delta B W_{JJ}^2/\Phi_0 = 1.70$. With the green open star symbol, we plot $\Delta B W_{JJ}^2/\Phi_0$ for the bar-shaped sample in Fig. 6. The error bars correspond to a 20-nm uncertainty in the junction length [30].

Another method of accounting for the influence of the notches is modifying the Fourier relation between the critical current density distribution $J(y)$ and the magnetic interference pattern $I_c(B)$, which will be discussed in the next section.

IV. FOURIER ANALYSIS OF THIN-FILM PLANAR JUNCTIONS

In their 1971 paper, Dynes and Fulton found a Fourier relation between the current density distribution of a Josephson junction and its magnetic interference pattern [16]. This method has been used widely in the last years in analyzing supercurrents in planar Josephson junctions [1,2,6–9,13,14,31–33]. However, the original Fourier relation is developed for macroscopic junctions where the screening currents are Meissner based. This section will give a brief review of the Dynes and Fulton method and will adapt the Fourier relation for use in thin-film planar junctions, which is essential for correctly interpreting interference patterns obtained on such junctions.

First we write the current phase relation in Eq. (11) as a complex expression and extend the integration bounds to infinity, since $J_c(y) = 0$, for $y > |W_{JJ}/2|$:

$$I(B) = \text{Im}\left(e^{i\varphi(0)}\int_{-\infty}^{\infty} J_c(y)e^{i\varphi_B}\, dy\right). \quad (19)$$

Here, φ_B is the gauge-invariant phase difference over the junction due to the magnetic induction. The critical current is given by the absolute value of the complex expression. Note that this is equal to setting $\varphi(0) = \pi/2$ in Eq. (12):

$$I_c(B) = \left|\int_{-\infty}^{\infty} J_c(y)e^{i\varphi_B(B,y)}\, dy\right|. \quad (20)$$

From this equation a general expression for a Fourier transform can be recognized. For a junction with macroscopic leads discussed above, we have $\varphi_B(B,y) = \frac{2\pi(2\lambda+d)B}{\Phi_0}y$ and therefore

$$I_c(\beta) = \left|\int_{-\infty}^{\infty} J_c(y)e^{2\pi i\beta y}\, dy\right|. \quad (21)$$

Here, we have defined the reduced field $\beta = \frac{(2\lambda+d)B}{\Phi_0}$, such that the position along the junctions y and β form conjugate variables. For the mesoscopic devices discussed here, this
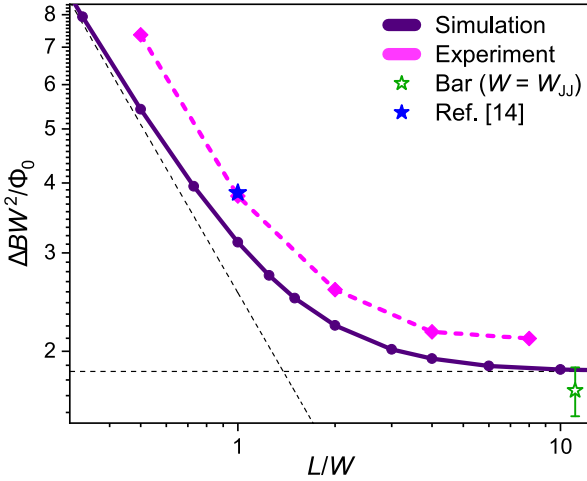
FIG. 6. Calculated periodicity ΔB of the fifth lobe of the interference pattern $I_c(B)$ obtained for the ellipse-shaped samples, compared with experimentally obtained values. We plot the dimensionless measure $\frac{\Delta B W^2}{\Phi_0}$ vs the aspect ratio L/W. The blue star indicates the periodicity of the cobalt-based disk junctions discussed in Ref. [14]. Although we predicted the L/W dependence, we find a constant offset between the experimental values and the simulations. This is due to the notches visible in Figs. 5(a) and 5(c), which makes the actual junction width (W_{JJ}) shorter than the width of the electrodes (W). To further illustrate this, we plot $\frac{\Delta B W_{JJ}^2}{\Phi_0}$ (open green star).

quantity needs to be replaced by Eq. (10), yielding

$$I_c(B) = \left| \int_{-\infty}^{\infty} J_c(y) e^{i2\gamma\left(\frac{d}{2}, y\right)} \, dy \right|, \tag{22}$$

where we omitted the contribution from the weak link, as its magnitude is negligible. Specifying $\gamma\left(\frac{d}{2}, y\right)$ using Eq. (14), we can define a new pair of conjugate variables—the length $\tilde{y} = W f\left(\frac{y}{W}\right)$ and the reduced field $\tilde{\beta} = \frac{7}{\pi^3} \frac{\zeta(3)}{\Phi_0} \frac{BW}{\Phi_0} \tanh\left(\frac{\pi^3}{28 \, \zeta(3)} \frac{A}{W^2}\right)$ [34]—to arrive at

$$I_c(\tilde{\beta}) = \left| \int_{-\infty}^{\infty} \tilde{J}_c(\tilde{y}) e^{i2\pi\tilde{\beta}\tilde{y}} \, d\tilde{y} \right|, \tag{23}$$

where we made a change of coordinates and $\tilde{J}_c$ is defined as

$$\tilde{J}_c\left(\frac{\tilde{y}}{W}\right) = \frac{dg}{d\tilde{y}}\left(\frac{\tilde{y}}{W}\right) J_c\left[W g\left(\frac{\tilde{y}}{W}\right)\right]. \tag{24}$$

Here, the function $g\left(\frac{\tilde{y}}{W}\right)$ is the inverse of $f\left(\frac{y}{W}\right)$, or $g\left(\frac{\tilde{y}}{W}\right) = f^{-1}\left(\frac{y}{W}\right)$. Equation (24) is a Fourier transform that includes a rescaling of the axes to retrieve the actual current density distribution $J_c(y)$.

In Fig. 7 we compare three different methods of obtaining the current density distribution extracted by the Fourier analysis from the data obtained on the disk-shaped sample shown in Fig. 5(b). Specifically, Fig. 7(a) shows the current density distribution obtained using the method for macroscopic junctions [i.e., following Eq. (21), using $L_{eff} = 2\lambda + d$] and Fig. 7(b) shows the Fourier transform based on our phase difference calculations [Eq. (22)]. The solid reference lines indicate the width of the electrodes (i.e., the disk diameter W), and the dashed reference lines indicate the width of the
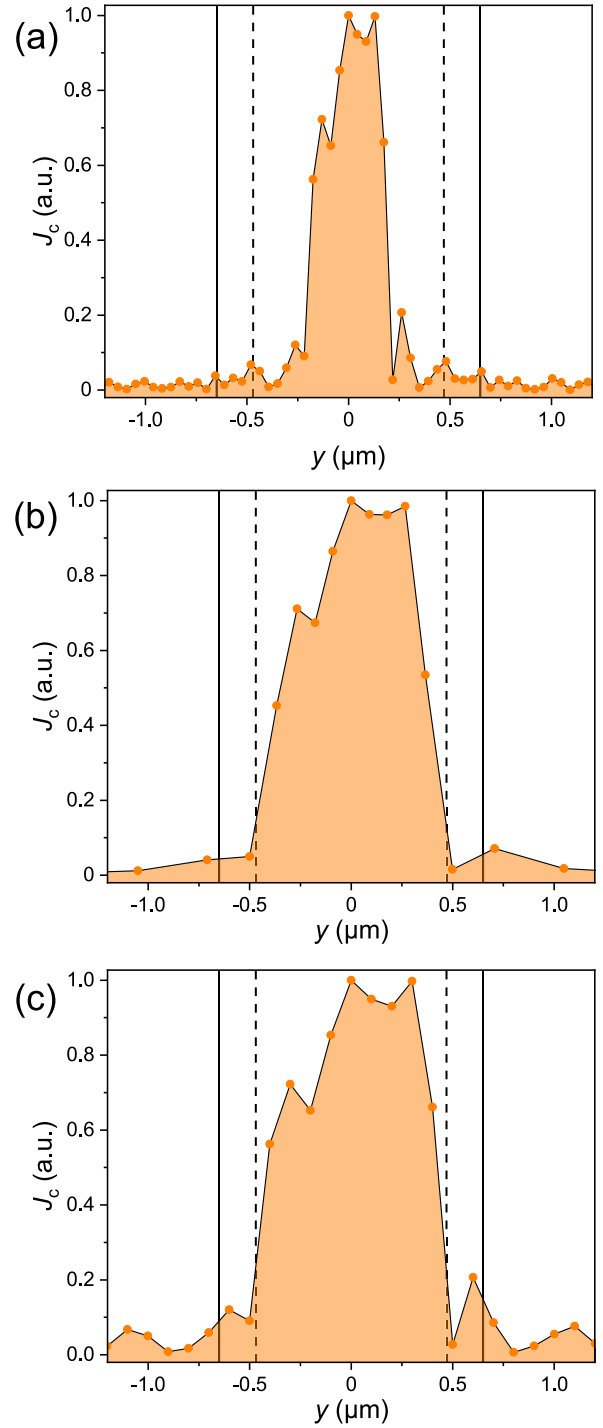

FIG. 7. Fourier analysis of the interference pattern shown in Fig. 5(b), carried out using three different methods. In (a) we use the formalism for macroscopic junctions [following Eq. (21), where $L_{eff} = 2\lambda + d$], whereas in (b), we make use of the simulation data shown in Fig. 2(b) [following Eq. (22)]. We indicate the boundaries of the electrodes ($-W/2$ and $W/2$) by solid reference lines and the boundaries of the actual weak link ($-W_{JJ}/2$ and $W_{JJ}/2$) by dashed reference lines. Only the method based on the simulations of the shielding currents correctly predicts the uniform current density distribution, which is limited to the actual junction only. Finally, in (c), we carry out the Fourier analysis using a linear approximation of $f_{disk}\left(\frac{y}{W}\right)$, circumventing the need for rescaling the axes, yet retaining the correct $J_c(y)$.

actual junction as measured from the scanning electron micrograph (W_{JJ}). We only observe a constant distribution of critical current throughout the full width of the junction (expected for uniform S-N-S junctions) when we incorporate the calculations presented in this paper. In contrast, the analysis based on $L_{eff} = 2\lambda + d$ yields an unphysical concentration of critical current in the middle of the junction. Finally, note that the current is confined to the actual junction (W_{JJ}), not the full width of the superconducting film (W). This explains the constant offset in Fig. 6.

Alternatively, we can use a linear approximation of $\gamma(\frac{d}{2}, y)$ to mitigate the need for rescaling the axes. Figure 7(c) shows the same Fourier analysis based on a linear approximation of $f(\frac{y}{W})$. Since the linear approximation of $f_{disk}(\frac{y}{W})$ breaks down near the edges, it yields less precise results at the junction boundaries. However, in the middle of the junction, the linear approximation of $f(\frac{y}{W})$ is well suited for correctly analyzing $J_c(y)$. For the technical details of carrying out the Fourier transform, the reader is referred to the Supplemental Material [26].

V. CONCLUSION

In conclusion, we analyzed the periodicity ΔB of the interference pattern $I_c(B)$ for thin-film planar S-N-S junctions, both theoretically and experimentally. Specifically, we examine junctions separating rectangular, ellipsoid, and rhomboid films of width W and length L. By mapping the second Ginzburg-Landau equation to the two-dimensional Laplace equation, we solve $I_c(B)$ for different ratios L/W. We show that ΔB has two universal limits for $L \gg W$ and $L \ll W$, independent of the sample geometry. The first corresponds to an infinite superconducting strip, and the latter is caused by an emerging universal dependence of the phase difference on the junction electrode surface area. By fabricating elliptically shaped S-N-S junctions, having different ratios L/W, we experimentally verify the geometry dependence of ΔB. Lastly, we adapt the Fourier relation between $I_c(B)$ and the critical current density distribution to suit planar junctions in the thin-film limit. This proves to be vital in correctly predicting the location of current channels in topological planar Josephson junctions.

ACKNOWLEDGMENTS

APPENDIX: DERIVATION OF THE BOUNDARY CONDITIONS

As discussed in the main text, the Neumann boundary conditions for the gauge-invariant phase are given by

$$(\nabla\gamma) \cdot \hat{\boldsymbol{n}}_R = -\frac{2\pi}{\Phi_0} \boldsymbol{A} \cdot \hat{\boldsymbol{n}}_R. \tag{A1}$$

In this Appendix, we will derive the results presented in Table I.

Combining the choice of the gauge $\boldsymbol{A} = -yB\hat{x}$ with $\hat{\boldsymbol{n}}_R = \hat{x}$ for boundary 1, we find

$$(\nabla\gamma) \cdot \hat{\boldsymbol{n}}_R = \left(-\frac{2\pi}{\Phi_0}\right)(-yB)\,\hat{x} \cdot \hat{x} = \frac{2\pi B}{\Phi_0}y. \tag{A2}$$

For boundary 2 we obtain the same result, yet with a minus sign since $\hat{\boldsymbol{n}}_R = -\hat{x}$. For boundary 3, $\hat{\boldsymbol{n}}_R = \pm\hat{y}$, which yields $(\nabla\gamma) \cdot \hat{\boldsymbol{n}}_R \sim \hat{x} \cdot \hat{y} = 0$.

Next, for boundary 4, parametrize the ellipse as $\frac{L}{2}\cos t\,\hat{x} + \frac{W}{2}\sin t\,\hat{y}$. The tangent is then given by the derivative to t, which is $-\frac{L}{2}\sin t\,\hat{x} + \frac{W}{2}\cos t\,\hat{y} = -\frac{Ly}{W}\hat{x}\frac{Wx}{L}\hat{y}$. Here, in the second step, we transformed back to Cartesian coordinates lying on the ellipse. A vector perpendicular to the tangent, pointing inwards to the ellipse, is then given by $-\frac{Wx}{L}\hat{x} - \frac{Ly}{W}\hat{y}$. Normalizing yields $\hat{\boldsymbol{n}}_R$:

$$\hat{\boldsymbol{n}}_R = -\frac{1}{\sqrt{\left(\frac{Wx}{L}\right)^2 + \left(\frac{Ly}{W}\right)^2}}\left(\frac{Wx}{L}\hat{x} + \frac{Ly}{W}\hat{y}\right). \tag{A3}$$

Taking the inner product with $\boldsymbol{A}$, as in Eq. (A2), yields the boundary condition in Table I. Finally, for boundary 5, define the angle α as $\arctan(W/L)$. In that case, for $y > 0$, we find $\hat{\boldsymbol{n}}_R = -\sin\alpha\,\hat{x} + -\cos\alpha\,\hat{y}$, such that

$$\hat{\boldsymbol{n}}_R = -\frac{1}{\sqrt{W^2 + L^2}}(W\hat{x} + L\hat{y}), \tag{A4}$$

again yielding the boundary condition in Table I. Note that the boundary condition is unchanged for $y < 0$, even though the y component of $\hat{\boldsymbol{n}}_R$ acquires a minus sign. This results from the choice of gauge ($A_y = 0$).

[1] S. Hart, H. Ren, T. Wagner, P. Leubner, M. Mühlbauer, C. Brüne, H. Buhmann, L. W. Molenkamp, and A. Yacoby, Induced superconductivity in the quantum spin Hall edge, Nat. Phys. **10**, 638 (2014).

[2] V. S. Pribiag, A. J. A. Beukman, F. Qu, M. C. Cassidy, C. Charpentier, W. Wegscheider, and L. P. Kouwenhoven, Edge-mode superconductivity in a two-dimensional topological insulator, Nat. Nanotechnol. **10**, 593 (2015).

[3] A. Fornieri, A. M. Whiticar, F. Setiawan, E. Portolés, A. C. C. Drachmann, A. Keselman, S. Gronin, C. Thomas, T. Wang, R. Kallaher, G. C. Gardner, E. Berg, M. J. Manfra, A. Stern, C. M.

Marcus, and F. Nichele, Evidence of topological superconductivity in planar Josephson junctions, Nature (London) **569**, 89 (2019).

[4] B. Mayer, S. Schuster, A. Beck, L. Alff, and R. Gross, Magnetic field dependence of the critical current in YBa$_2$Cu$_3$O$_{7-\delta}$ bicrystal grain boundary junctions, Appl. Phys. Lett. **62**, 783 (1993).

[5] S. A. Cybart, E. Y. Cho, T. J. Wong, B. H. Wehlin, M. K. Ma, C. Huynh, and R. C. Dynes, Nano Josephson superconducting tunnel junctions in YBa$_2$Cu$_3$O$_{7-\delta}$ directly patterned with a focused helium ion beam, Nat. Nanotechnol. **10**, 598 (2015).

[6] J. Ying, J. He, G. Yang, M. Liu, Z. Lyu, X. Zhang, H. Liu, K. Zhao, R. Jiang, Z. Ji, J. Fan, C. Yang, X. Jing, G. Liu, X. Cao, X. Wang, L. Lu, and F. Qu, Magnitude and spatial distribution control of the supercurrent in Bi$_2$O$_2$Se-based Josephson junction, Nano Lett. **20**, 2569 (2020).

[7] B. H. Elfeky, N. Lotfizadeh, W. F. Schiela, W. M. Strickland, M. Dartiailh, K. Sardashti, M. Hatefipour, P. Yu, N. Pankratova, H. Lee, V. E. Manucharyan, and J. Shabani, Local control of supercurrent density in epitaxial planar Josephson junctions, Nano Lett. **21**, 8274 (2021).

[8] M. T. Allen, O. Shtanko, I. C. Fulga, A. R. Akhmerov, K. Watanabe, T. Taniguchi, P. Jarillo-Herrero, L. S. Levitov, and A. Yacoby, Spatially resolved edge currents and guided-wave electronic states in graphene, Nat. Phys. **12**, 128 (2016).

[9] M. Fortin-Deschênes, R. Pu, Y.-f. Zhou, C. Ma, P. Cheung, K. Watanabe, T. Taniguchi, F. Zhang, X. Du, and F. Xia, Uncovering topological edge states in twisted bilayer graphene, Nano Lett. **22**, 6186 (2022).

[10] T. Golod, O. M. Kapran, and V. M. Krasnov, Planar Superconductor-Ferromagnet-Superconductor Josephson Junctions as Scanning-Probe Sensors, Phys. Rev. Appl. **11**, 014062 (2019).

[11] J. C. LeFebvre, E. Cho, H. Li, H. Cai, and S. A. Cybart, Flux focused series arrays of long Josephson junctions for high-dynamic range magnetic field sensing, J. Appl. Phys. **131**, 163902 (2022).

[12] R. A. Hovhannisyan, T. Golod, and V. M. Krasnov, Holographic reconstruction of magnetic field distribution in a Josephson junction from diffraction-like $I_c(H)$ patterns, Phys. Rev. B **105**, 214513 (2022).

[13] K. Lahabi, M. Amundsen, J. A. Ouassou, E. Beukers, M. Pleijster, J. Linder, P. Alkemade, and J. Aarts, Controlling supercurrents and their spatial distribution in ferromagnets, Nat. Commun. **8**, 2056 (2017).

[14] R. Fermin, D. van Dinter, M. Hubert, B. Woltjes, M. Silaev, J. Aarts, and K. Lahabi, Superconducting triplet rim currents in a spin-textured ferromagnetic disk, Nano Lett. **22**, 2209 (2022).

[15] K. R. Jeon, B. K. Hazra, K. Cho, A. Chakraborty, J. C. Jeon, H. Han, H. L. Meyerheim, T. Kontos, and S. S. Parkin, Long-range supercurrents through a chiral non-collinear antiferromagnet in lateral Josephson junctions, Nat. Mater. **20**, 1358 (2021).

[16] R. C. Dynes and T. A. Fulton, Supercurrent density distribution in Josephson junctions, Phys. Rev. B **3**, 3015 (1971).

[17] J. Pearl, Current distribution in superconducting films carrying quantized fluxoids, Appl. Phys. Lett. **5**, 65 (1964).

[18] Y. Ivanchenko and T. Soboleva, Nonlocal interaction in Josephson junctions, Phys. Lett. A **147**, 65 (1990).

[19] A. A. Abdumalikov, Jr., G. L. Alfimov, and A. S. Malishevskii, Nonlocal electrodynamics of Josephson vortices in superconducting circuits, Supercond. Sci. Technol. **22**, 023001 (2009).

[20] A. A. Boris, A. Rydh, T. Golod, H. Motzkau, A. M. Klushin, and V. M. Krasnov, Evidence for Nonlocal Electrodynamics in Planar Josephson Junctions, Phys. Rev. Lett. **111**, 117002 (2013).

[21] V. G. Kogan, V. V. Dobrovitski, J. R. Clem, Y. Mawatari, and R. G. Mints, Josephson junction in a thin film, Phys. Rev. B **63**, 144501 (2001).

[22] M. Moshe, V. G. Kogan, and R. G. Mints, Edge-type Josephson junctions in narrow thin-film strips, Phys. Rev. B **78**, 020510(R) (2008).

[23] J. R. Clem, Josephson junctions in thin and narrow rectangular superconducting strips, Phys. Rev. B **81**, 144515 (2010).

[24] D. Rodan-Legrain, Y. Cao, J. Park, S. de la Barrera, T. Mallika, K. Watanabe, T. Tanigushi, and P. Jarillo-Herrero, Highly tunable junctions and non-local Josephson effect in magic-angle graphene tunnelling devices, Nat. Nanotechnol. **16**, 769 (2021).

[25] Here, we assume a weak Josephson current, such that the magnitude of the superconducting order parameter is not suppressed and is given by the equilibrium value.

[26] See Supplemental Material at http://link.aps.org/supplemental/10.1103/PhysRevB.107.064502 for the COMSOL application file containing the simulations, a description of the technical details of the Fourier transform, and results obtained on the bar-shaped sample.

[27] R. Fermin, N. M. A. Scheinowitz, J. Aarts, and K. Lahabi, Mesoscopic superconducting memory based on bistable magnetic textures, Phys. Rev. Res. **4**, 033136 (2022).

[28] Figures 5(a) and 5(b) are used as a control experiment in Ref. [14]; the data are presented in the Supporting Information of that paper.

[29] S. Mandal, S. Dutta, S. Basistha, I. Roy, J. Jesudasan, V. Bagwe, L. Benfatto, A. Thamizhavel, and P. Raychaudhuri, Destruction of superconductivity through phase fluctuations in ultrathin *a*-MoGe films, Phys. Rev. B **102**, 060501(R) (2020).

[30] We assume a relatively high uncertainty in the junction length due to the superconducting electrodes shielding the line of sight to the junction, which makes establishing W_{JJ} more difficult. Furthermore, we have used $\Delta B = \Delta B_4$ since a rapid decay of the $I_c(B)$ pattern prevented establishing ΔB_5. It must be noted that the average over the periodicity of the side peaks yields $\Delta B W_{JJ}^2/\Phi_0 = 1.83$.

[31] C. Huang, B. T. Zhou, H. Zhang, B. Yang, R. Liu, H. Wang, Y. Wan, K. Huang, Z. Liao, E. Zhang, S. Liu, Q. Deng, Y. Chen, X. Han, J. Zou, X. Lin, Z. Han, Y. Wang, K. T. Law, and F. Xiu, Proximity-induced surface superconductivity in Dirac semimetal Cd$_3$As$_2$, Nat. Commun. **10**, 2217 (2019).

[32] H. J. Suominen, J. Danon, M. Kjaergaard, K. Flensberg, J. Shabani, C. J. Palmstrøm, F. Nichele, and C. M. Marcus, Anomalous Fraunhofer interference in epitaxial superconductor-semiconductor Josephson junctions, Phys. Rev. B **95**, 035307 (2017).

[33] F. K. de Vries, T. Timmerman, V. P. Ostroukh, J. van Veen, A. J. A. Beukman, F. Qu, M. Wimmer, B.-M. Nguyen, A. A. Kiselev, W. Yi, M. Sokolich, M. J. Manfra, C. M. Marcus, and L. P. Kouwenhoven, h/e Superconducting Quantum Interference through Trivial Edge States in InAs, Phys. Rev. Lett. **120**, 047702 (2018).

[34] Naturally, any choice of $\tilde{y}$ and $\tilde{\beta}$ is allowed, as long as it is consistent with γ.